scientific reports

OPEN

Investigating the impact of electron beam irradiation on electrical, magnetic, and optical properties of XLPE/Co$_3$O$_4$ nanocomposites

Mohamed Mohamady Ghobashy[1✉], A. I. Sharshir[2✉], R. A. Zaghlool[2] & F. Mohamed[3]

Nowadays, many researchers aim to fill polymer materials with inorganic nanoparticles to enhance the polymer properties and gain the merits of the polymeric host matrix. Sol–gel synthesized Co$_3$O$_4$ nanoparticles are subjected to different doses of electron beam (10, 20, and 30 kGy) to study their physiochemical properties and choose the optimized nanoparticles to fill our polymeric matrix. Crosslinked polyethylene (XLPE) has been filled with 5 wt % of un-irradiated cobalt oxide nanoparticles using the melt extruder method. The structural, optical, magnetic, and electrical properties of the XLPE/Co$_3$O$_4$ nanocomposite before and after exposure to different doses of electron beam radiation have been characterized. The crystallite size of face-centered cubic spinel Co$_3$O$_4$ nanoparticles has been confirmed by XRD whereas and their unique truncated octahedral shape obviously appears in SEM micrographs. The crystallite size of Co$_3$O$_4$ nanoparticles has decreased from 47.5 to 31.5 nm upon irradiation at a dose of 30 kGy, and significantly decreased to 18.5 nm upon filling inside XLPE matrix. Related to the oxidation effect of the electron beam, the Co^{2+}/Co^{3+} ratio on the surface of Co$_3$O$_4$ nanoparticles has decreased upon irradiation as verified by XPS technique. This consequently caused the partial elimination of oxygen vacancies, mainly responsible for the weak ferromagnetic behavior of Co$_3$O$_4$ in its nanoscale. This appears as decreased saturation magnetization as depicted by VSM. The XLPE/Co$_3$O$_4$ nanocomposite has also shown weak ferromagnetic behavior but the coercive field (H$_c$) has increased from 112.57 to 175.72 G upon filling inside XLPE matrix and decreased to 135.18 G after irradiating the nanocomposite at a dose of 30 kGy. The ionic conductivity of XLPE has increased from 0.133 × 10^{-7} to 2.198 × 10^{-3} S/cm upon filling with Co$_3$O$_4$ nanoparticles while a slight increase is observed upon irradiation.

Keywords Crosslinked polyethylene, Co$_3$O$_4$, Nanocomposites, Optical properties, Magnetic properties, Electrical properties

In recent decades, pursuing advanced materials with tailored properties has driven scientific and techno-logical research[1–7]. Nanocomposites, composed of nanoscale components dispersed within a matrix, have garnered significant attention due to their remarkable combination of properties that can surpass those of their constituents[8–15]. Integrating nanoparticles into polymer matrices has emerged as a promising avenue for achieving enhanced mechanical, electrical, magnetic, and optical characteristics among the diverse range of nanocomposites[16–21]. In particular, incorporating metal oxide nanoparticles into polymers has attracted signifi-cant interest in electronics and energy storage applications.

Cross-linked polyethylene (XLPE) is a cost-effective, highly flexible, thermally and chemically stable poly-mer characterized by good dielectric properties, low conductivity, and easy processing, frequently used as cable insulation material[22–24]. For these merits, filling XLPE with nanoparticles to modify its properties is frequently reported. XLPE/silica nanocomposites were prepared by Sharad et al. using twin screw extruder and injec-tion molding and they proved higher thermal stability upon surface modification by octylsilane[25]. Wang et al.

[1]Radiation Research of Polymer Chemistry Department, National Center for Radiation Research and Technology (NCRRT), Egyptian Atomic Energy Authority (EAEA), Cairo, Egypt. [2]Solid State and Electronic Accelerators Department, National Center for Radiation Research and Technology (NCRRT), Egyptian Atomic Energy Authority (EAEA), Cairo, Egypt. [3]Spectroscopy Department, Physics Research Institute, National Research Centre, 33 El Bohouth St., Dokki 12622, Giza, Egypt. ✉email: mohamed_ghobashy@yahoo.com; a.shr88@yahoo.com; ahmed.sharshir@eaea.org.eg

studied the effect of nanoparticle surface modification and filling concentration on space charge characteristics in TiO_2/XLPE nanocomposites[22]. Madani et al. have also investigated the dielectric behavior of XLPE/$BaTiO_3$ nanocomposites in the low-frequency range where the resultant nanocomposite show increased dielectric permittivity and highly decreased loss factor[26]. Mohamed et al. have investigated the electrical treeing behavior in XLPE insulation as it filled with Al_2O_3 nanoparticles and they observed higher time for treeing growth in XLPE insulation so extended cable life could be achieved[23]. Sharshir et al.[27] have prepared XLPE and its nanocomposite filled with ZnO nanoparticles which showed improvement of the electric field distribution in medium-voltage cables whereas Wang et al. have verified modified charge transport mechanism of the cable joint as XLPE has doped with MgO nanoparticles[28]. However, no studies are explored on the capability of filling XLPE with magnetic nanoparticles to impart it with magnetic characteristics which would be consequently applied in magnetic systems and spintronics.

Cobalt oxide (Co_3O_4) has garnered significant attention among metal oxides due to their intriguing magnetic, catalytic, and electronic properties. Co_3O_4 is a reasonably priced[29] antiferromagnetic[30] versatile semiconductor[31] with a unique crystal structure that can influence its electrical and magnetic behavior[32–34]. Co_3O_4 can be prepared in nanosized form with controllable shape and dimension with amazing optical and magnetic properties which could be applied in memory devices, electrical switching and microwave devices. In contrast to its bulk form, the nanosized Co_3O_4 shows weak ferromagnetism or superparamagnetism[35,36]. In addition to their ferromagnetic behavior, previous studies have highlighted the distinctive attributes of Co_3O_4 nanoparticles, including high surface area, and potential for catalytic applications. One intriguing aspect of Co_3O_4 is the presence of oxygen vacancies – lattice defects in which oxygen atoms are missing from the crystal structure. Oxygen vacancies can give rise to intriguing phenomena, including alterations in electronic structure, magnetism, and catalytic activity[37–40]. These vacancies introduce localized energy levels within the material's band structure, influencing charge transport and electronic behavior. As a result, oxygen vacancies have garnered significant attention for their potential to modulate material properties and enable new functionalities. So incorporating Co_3O_4 nanoparticles into polymer matrices introduces opportunities to engineer and tailor their properties for optical[41], optoelectronic[42], electrical, magnetic, and catalysis applications[43,44].

Many studies on the physical properties of polymer/Co_3O_4 nanocomposites have been reported in this context. PVDF/Co_3O_4 nanocomposite was prepared by Bhatt et al.[45] using spincoating method to enhance the polymer's conductivity and donating magnetic behavior to the matrix. Nandapure et al. have studied the effect of Co_3O_4 nanoparticles that prepared using sol–gel method on the magnetic behavior of polyaniline where the PANI/Co_3O_4nanocompositewas prepared using in-situ chemical oxidation polymerization of aniline using APS as an oxidant in the presence of Co_3O_4 nanoparticles in air at room temperature[46]. Wassel et al. have synthesized Co_3O_4 nanoparticles using the thermal decomposition method and investigated the morphological, optical, and magnetic properties of Co_3O_4/PANI nanocomposite prepared via in situ oxidative polymerization[47]. PANI/Co_3O_4 nanocomposite was also produced by Fan et al.[48] using in-situ polymerization technique and exhibited great electrochemical performance. Nanocomposites films of PANI-CSA/Co_3O_4 NPs were deposited on ITO-glass substrates by Al-Gharram et al. using the electrochemical polymerization method and the structural and optical properties have been investigated[30]. However, preparing XLPE/Co_3O_4 nanocomposite and investigating its physical properties have not been explored.

Electron beam irradiation presents a powerful method for inducing controlled structural modifications in materials, offering a means to precisely manipulate properties. Through controlled exposure to electron beams, it is possible to control oxygen vacancies within metal oxide nanoparticles, leading to intriguing changes in material behavior. This introduces a compelling avenue for tuning material properties through the controlled introduction or removal of defects, providing a deeper understanding of the underlying physics and chemistry at the nanoscale[27,49–52].

In this context, the present study delves into the effects of electron beam irradiation on the structural, optical, and magnetic properties of Co_3O_4 nanoparticles, prepared via the sol–gel method, and XLPE/Co_3O_4 nanocomposites as well as exploring the conductivity and dielectric properties of XLPE/Co_3O_4 nanocomposites. The interplay between these properties and the role of oxygen vacancies, surface cationic states, defects, and crystal lattice distortions are systematically explored.

The outcomes of this research hold significant implications for various technological applications. By tailoring the properties of XLPE/Co_3O_4 nanocomposites through controlled electron beam irradiation, the resulting materials can be optimized for specific uses, such as electrical insulation, energy storage, and magnetic devices. Furthermore, the insights gained from this study can contribute to the fundamental understanding of the interactions between nanoparticles and polymers, paving the way for designing advanced nanocomposite materials with tailored functionalities.

Experimental
Materials
Cobalt (II) acetate tetrahydrate, with the chemical formula $(CH_3COO)_2Co·4H_2O$ and a molecular weight of 249.08, as well as Oxalic acid (HO_2CCO_2H) with a molecular weight of 90.03, were obtained from Sigma Aldrich Co. Elsewedy Electric Company supplied the XLPE material.

Preparation of Co_3O_4 nanocomposite and *e*-beams irradiation process
A typical experiment created Co_3O_4 nanoparticles using the traditional sol–gel process. Solution A of the salt was created by dissolving 20.196 g (0.10 mol) of cobalt acetate in 600 mL of water/ethanol in a ratio 80/20 v/v% and stirring it for 60 min at room temperature. A solution of 0.20 mol of oxalic acid dehydrates was obtained by dissolving 2.520 g in 800 mL of water/ethanol in a ratio of 80/20 v/v% and stirred at a temperature of 50 °C for

60 min to create Solution B. Warm solution A was constantly mixed for one hour while solution B was added dropwise. A white sol was obtained, aged to create a gel, and then dried for 24 h at 100 °C. Co_3O_4 was finally produced using thermal processing at calcination temperatures of 600 °C. The obtained dried powder of Co_3O_4 was subsequently mixed with the appropriate amount of H_2O_2 (20%) for 120 min. After that, the mixture of (Co_3O_4 and H_2O_2) was dried in an oven at a temperature of 250 °C. After 3 h, the black precipitate of (Co_3O_4) was washed with de-ionized water and calcination at a muffle furnace at a temperature of 900 °C for 2 h before being subject to e-beam at doses of (0, 10, 20 and 30 kGy).

Preparation of XLPE/Co₃O₄ by melt extruder method

The cross-linked polyethylene (XLPE) pellets were sourced from El Sewedy Electricity Company in Egypt, originally intended to manufacture high voltage (HV) cables with a rate 33 kV. The XLPE material was melted at 160 °C to initiate the composite fabrication process, utilizing a twin-screw extruder (CTW100P; Haake PolyLab RheoMix, Germany). Concurrently, Co_3O_4 nanoparticles, constituting 5 wt% and exposed to doses of 0, 10, 20, and 30 kGy, were introduced into the molten XLPE in its un-irradiated form and meticulously blended within the extruder. This amalgamation was achieved by maintaining a screw speed of 120 rpm for 7 min, ensuring thorough dispersion of the nanoparticles throughout the polymer matrix. After the extrusion stage, the composite mixture was subjected to compression-molding procedures utilizing a specialized hot press apparatus (Lab Tech Engineering Co., Bangkok, Thailand). During compression molding, the temperature was regulated at 170 °C, and a substantial pressure of 150 kg/cm² was applied for 4 min. This rigorous molding process consolidated the XLPE/Co_3O_4 composite into a well-defined form. Upon completion of the molding procedure, the resultant XLPE/Co_3O_4 composite was meticulously sectioned into test specimens, each measuring 2×2 cm in dimensions. These prepared test pieces were then designated for subsequent rounds of comprehensive experimental assessments to elucidate and evaluate the material's multifaceted properties and behaviors, particularly in light of its exposure to different electron beam irradiation doses. The precise and controlled manufacturing protocol outlined above underscores the meticulous approach to creating the XLPE/Co_3O_4 composite specimens, ensuring uniformity and consistency in their composition and structure for subsequent scientific investigations and analyses.

e-beams process

A linear particle accelerator (Vivi rad company, France) of 3.0 MeV electron flux with 30 mA at rated current and convyier speed 16 m/min was used to irradiate the samples. The dimension of source electron beam accelerator was (80×70) cm. The minimum dose was 3 kGy. The dose rate depended on convyier speed and current. The films were irradiated at ambient temperature by accelerated electrons until the absorbed doses from 10 to 30 kGy were reached.

Measurements

The morphology of Co_3O_4 nanoparticles was examined by SEM EISS—EVO 15- UK scanning electron microscope at an accelerating voltage of 25 kV. Furthermore, the morphology and structures of the samples were investigated using transmission electron microscopy (TEM) with a JEOL-2010 instrument from Japan, providing detailed information about the nanoscale features and arrangement of the materials. XRD analysis was accomplished using SHIMADZU XRD 6000, operating at 1200 W, using the Cu-Kα radiation ($\lambda = 1.5406$ Å), 2θ ranges from 4 to 90. Unpaired electron analysis was achieved using BRUKER EMX EPR spectrometer whereas JASCO V-570 spectrophotometer was used to measure the diffused reflectance of Co_3O_4 nanoparticles and XLPE/Co_3O_4 nanocomposite in the spectral range from 190 to 2500 nm. For photoluminescence measurement, (SF-Jasco-FP-6500, Japan) spectrofluorometer was used and the samples were excited at 250 nm (laser diode) where the excitation slit band width was 5 nm. To explore the cationic oxidation states on the surface of Co_3O_4 nanoparticles, X-Ray photoelectron spectrometer (XPS) Thermo Scientific K-ALPHA instrument was used. The magnetic analysis was accomplished using Lake Shore 7410 Vibrating Sample Magnetometer (VSM). The dielectric measurements were carried out in the frequency range 10^{-1} to 10^7 Hz at room temperature by employing Alpha-A machine from novocontrol. Samples were irradiated with 3 MeV electron beam at different dose (10, 20, and 30 kGy) at room temperature by Vivi rad (France) industrial linear electron accelerator in NCRRT, Egyptian Atomic Energy Authority. The conveyor speed is 16 m/min and the current was 30 mA.

Quantification of physical parameters influenced by *e*-beam irradiation of Co₃O₄ nanoparticles and XLPE/Co₃O₄ nanocomposite

Electron beam (e-beam) irradiation has gained significant attention as a versatile technique for modifying the properties of materials at the nanoscale. In nanomaterials, cobalt oxide (Co_3O_4) is a promising compound with applications ranging from catalysis to energy storage. This study delves into the effects of e-beam irradiation on Co_3O_4 nanoparticles and XLPE/Co_3O_4 nanocomposite, aiming to quantify changes in various physical parameters.

X-ray diffraction (XRD) analysis
XRD analysis is a powerful technique for probing crystallographic information and quantifying various structural characteristics. The following equations were employed to derive essential parameters:

<u>Crystallite size calculation.</u>   The crystallite size (D) was calculated utilizing Scherrer's equation[53]:

$$D = \frac{K\lambda}{\beta \cos\theta}, \tag{1}$$

where D represents the crystallite size, K is a constant (K = 0.94), λ denotes the wavelength of X-rays used, θ corresponds to the Bragg's angle, and β signifies the full width at half maximum.

Unit cell length (a) calculation.   The unit cell length (a) was determined based on the cubic structure of Co_3O_4 using the relation[54,55]:

$$\frac{1}{d^2} = \frac{h^2 + k^2 + 1^2}{a^2}, \tag{2}$$

Here, h, k, and l are the Miller indices associated with the crystal lattice.

Dislocation density calculation.   The dislocation density (δ) was calculated using the formula[56,57]:

$$\delta = \frac{1}{D^2}, \tag{3}$$

where δ represents the dislocation density and D is the crystallite size.

Optical band gap estimation
The optical band gap, a crucial parameter governing the material's light absorption behavior, was estimated using the Kubelka–Munk function. The equation utilized is as follows:

Kubelka–Munk function.   The Kubelka–Munk function (F(R%)) was employed for optical band gap estimation[58]:

$$F(R\%) = \frac{(1 - R\%)^2}{2R\%}, \tag{4}$$

R% denotes the diffused reflectance, and F(R%) is the Kubelka–Munk function.

Impedance spectroscopic study
Impedance spectroscopy offers insights into the electrical properties of materials, particularly their conductivity. The following equation was used to quantify DC conductivity:

DC conductivity calculation.   The DC conductivity (σ) was calculated using the equation[59–61]:

$$\sigma = \frac{L}{R_b \times A}, \tag{5}$$

where σ represents the DC conductivity, L denotes the membrane thickness, A signifies the area, and R_b is the bulk resistance.

The meticulous application of these equations enabled the determination of critical physical parameters, contributing to a comprehensive characterization of the materials under investigation. By quantifying these parameters, the study advances our understanding of the materials' structural, optical, and electrical properties, paving the way for potential applications and further scientific insights.

Results and discussion
The physiochemical properties of *e*-beam irradiated Co_3O_4 nanoparticles
The physicochemical properties of the electron beam (*e*-beam) irradiated Co_3O_4 nanoparticles refer to the changes and characteristics observed in the Co_3O_4 nanoparticles after they have been subjected to e-beam irradiation. This irradiation process can induce modifications in various aspects of the nanoparticles' structure and behavior.

SEM and TEM analysis
Figure 1a shows SEM image of the as-prepared Co_3O_4 nanoparticles, mostly composed of truncated octahedrons (enclosed by [100] and [111] facets) with edge lengths ranging from 20 to 150 nm. The size of the Co_3O_4 cube particle is non-uniform, as depicted in Fig. 1a, which shows some irregular Co_3O_4, including the grains that are recombined in the nanoparticles products are formed. In Fig. 1b we can see some truncated octahedrons agglomeration particles. There is almost coercivity attraction for Co_3O_4 nanoparticles, which is a very typical behavior for a soft magnet[62]. This intriguing behavior, often associated with materials possessing low coercivity values, underscores the unique magnetic properties of the Co_3O_4 nanoparticles within the system under study. The fact that the Co_3O_4 nanoparticles in the study exhibit a strong tendency to cluster together due to their mutual magnetic attraction suggests that these nanoparticles possess low coercivity. This low coercivity is a typical behavior of soft magnetic materials and is significant because it indicates the unique magnetic properties of the Co_3O_4 nanoparticles in the investigated system. Figure 1c and 1d show the TEM image of Co_3O_4 in the nanoscale with non-uniform cubic shape.
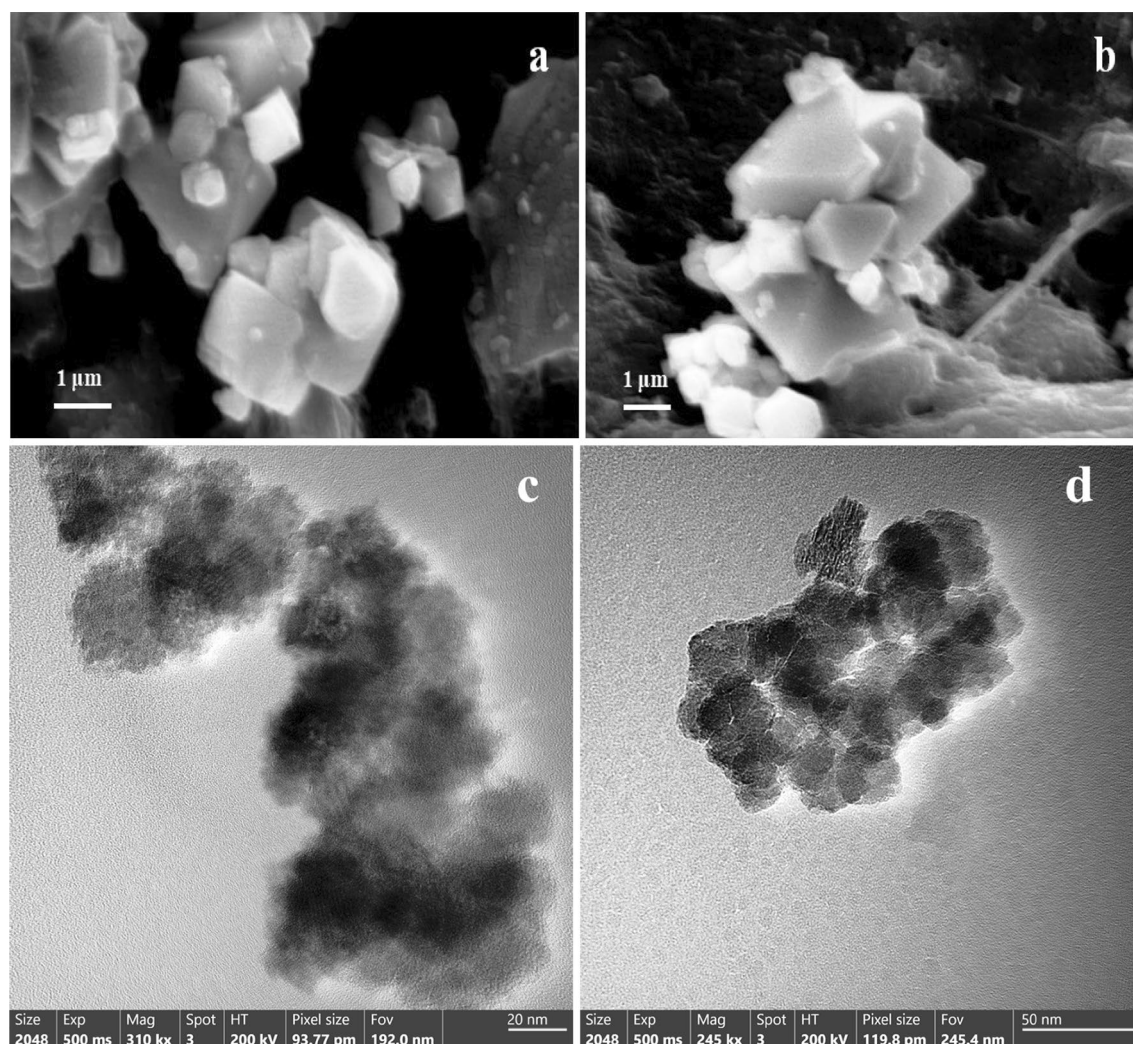
Figure 1. SEM images of the as prepared Co_3O_4 nanoparticles at two magnification levels where: (**a**) 10000x, (**b**) 8000x, and TEM images at: (**c**) 20 nm and (**d**) 50 nm levels.

XRD analysis

Figure 2a shows a characteristic XRD pattern of the cubic phase of Co_3O_4 with a spinel structure. The XRD planes of cobalt oxide before irradiation appear at 2θ values 18.79°, 31.04°, 36.63°, 38.31°, 44.58°, 55.74°, 59.15°, 65.01° and 76.57° which are related to (111), (220), (311), (400), (511), (222), (440) and (533) diffraction planes of face-centered cubic spinel Co_3O_4, respectively. This is in agreement with JCPDS Card No. 42-1467. The observed peaks matching the Bragg reflections of the standard face-centered cubic (fcc) structure. No other phases, such as the hexagonal CoO wurzite is discernible. As the dose increases from 0 to 10 kGy and then 30 kGy, the crystallite size of the Co_3O_4 nanoparticles decreases from 47.55 to 18.50 nm and then 31.51 nm, respectively. This indicates a decrease in crystallinity with higher *e*-beams doses. However, at an intermediate dose of 20 kGy, the crystallite size increases to 51.26 nm, while the dislocation density decreases. This suggests that the nanoparticles exposed to 20 kGy have higher crystallinity compared to the residue Co_3O_4 nanoparticles. The highest dislocation density (2.921×10^{15} Lines/m^2) is observed for the nanoparticles exposed to 10 kGy, indicating the most distorted crystal structure at this dose (Table 1). The lowest dislocation density (0.38×10^{15} Lines/m^2) is observed for the nanoparticles exposed to 20 kGy, suggesting a more ordered crystal structure at this intermediate dose.

Figure 2b shows the XRD of cobalt oxide before and after irradiation by different e-beam doses (0, 10, 20, and 30 kGy). The peaks of [111] plane observed in the XRD patterns show little shift and different intensities correspond to specific crystallographic planes within the Co_3O_4 crystal lattice. These can reveal alterations in the arrangement of atoms within the crystal structure after exposure to *e*-beams. Figure 2b shows the changing of growth orientation-controlled (111) under the influence of *e*-beam. As observed, the *e*-beams doses cause the increase of (111) intensity with the shift in the position of 2θ to confirm the growth rate of (111) by *e*-beams irradiation. More interestingly, in Fig. 2a it is revealed that the increase of *e*-beams doses leads to alteration of the intensity of (311) plane as a preferred orientation of Co_3O_4 nanocrystals.

Furthermore, the decrease in crystal size for (311) plane was found with the growth in the crystal size for (111) plane. These findings provide an approach to the orientation-controllable Co_3O_4 nanocrystals of (111) plane as subjected to *e*-beams. This could be ascribed to the different spins of electrons which result in a redistribution
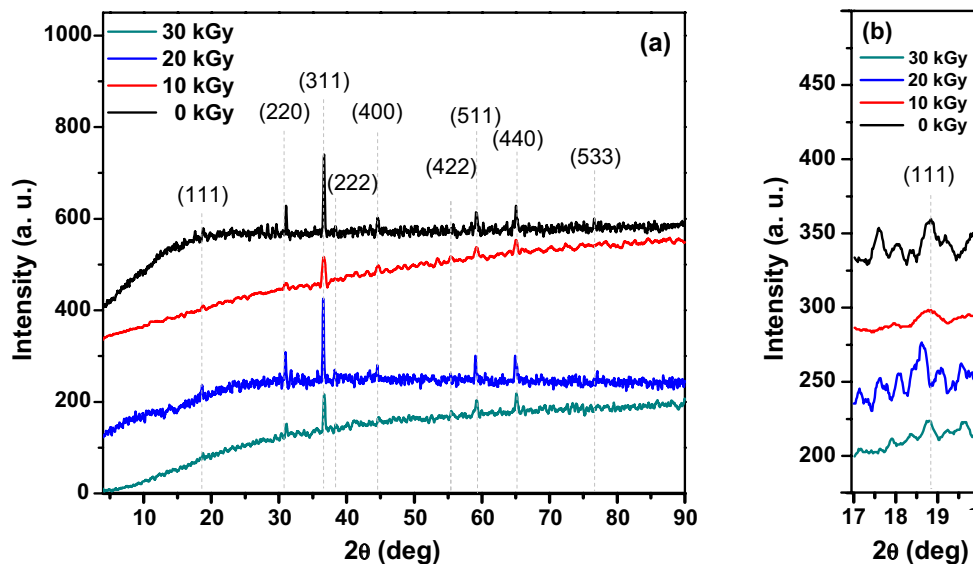
Figure 2. (**a**) The XRD patterns of Co_3O_4 before and after irradiation by different doses of electron beam and (**b**) the effect of radiation dose on the (111) plane growth.

Sample	D (nm)	a (A°)	$\delta \times 10^{15}$ (Lines/m²)
Co_3O_4 (0 kGy)	47.55	8.128	0.442
Co_3O_4 (10 kGy)	18.50	8.138	2.921
Co_3O_4 (20 kGy)	51.26	8.154	0.380
Co_3O_4 (30 kGy)	31.51	8.121	1

Table 1. XRD calculated parameters of Co_3O_4 nanoparticles before and after irradiation by different doses of electron beam.

of the density of states of the exposed nanoparticlesas a whole and can affect the magnetic properties of the Co_3O_4[63]. Since the catalytic reactions are affected by crystal facets according to their adsorption energies as well as the ability to transfer electrons, we followed the growth of (111) plane, which is entirely occupied by Co^{2+} ions and is reported to be responsible for the high catalytic performance of Co_3O_4 nanoparticles[64–66]. As shown in Fig. 2b, Co_3O_4 nanoparticles exposed to 20 kGy show the highest peak intensity of (111) plane whereas the Co_3O_4 nanoparticles exposed to 10 kGy show the lowest. Besides, the intensity of (111) plane of the irradiated Co_3O_4 nanoparticles at a dose of 30 kGy has been decreased compared to the un-irradiated Co_3O_4 nanoparticles. It is reported that while Co^{3+} ions change their positions, the Co^{2+} ions occupy the lattice point of (111) facet[67,68] which is responsible for the magnetic behavior of Co_3O_4 nanoparticles[69]. Relating to the oxidation effect of electron beams[70,71], some of Co^{2+} ions on the surface could be converted to Co^{3+} ions, consequently affecting the magnetic behavior of Co_3O_4 nanoparticles. It is also reported that the different crystal facets possess different adsorption energies and electron transfer properties, which might directly influence the catalytic reaction and ionic conductivity of Co_3O_4 nanoparticles[65]. So, the XRD results suggest that the orientation-controlled (111) Co_3O_4 nanocrystals could change the materials' magnetic and electrical properties.

Optical analysis for Co_3O_4 nanoparticles

The change in the absorption and the emission properties and the variation in the band gap of the nanoparticles may be due to the quantum confinement effect associated by alteration of crystallite size and shape as well as defects induced by radiation that could initiate localized states which affect the absorption as well as emission characteristics of the nanoparticles[72].

Optical band gap. The optical band gap (E_g) of Co_3O_4 nanoparticles (before and after irradiation by 30 kGy of electron beam) has been estimated from the diffused reflectance spectra using Kubelka–Munk function (Eq. 4). By plotting $(F(R) h\upsilon)^2$ versus $h\upsilon$ and extrapolating the linear part of the curve to $F(R)=0$, the optical band gap value of the samples could be determined. As revealed from Fig. 3, Co_3O_4 nanoparticles show two direct optical transitions before and after electron beam irradiation. This could be attributed to its electronic band structure; As cobalt ion has two oxidation states (Co^{3+} and Co^{2+}) there would be two associated charge transitions (O^{2-} to Co^{3+} and O^{2-} to Co^{2+}) which are responsible for the lower and higher optical absorption bands, respectively. For the un-irradiated Co_3O_4, the lower one is at 1.671 eV whereas the higher one is at 3.517 eV. These values agree
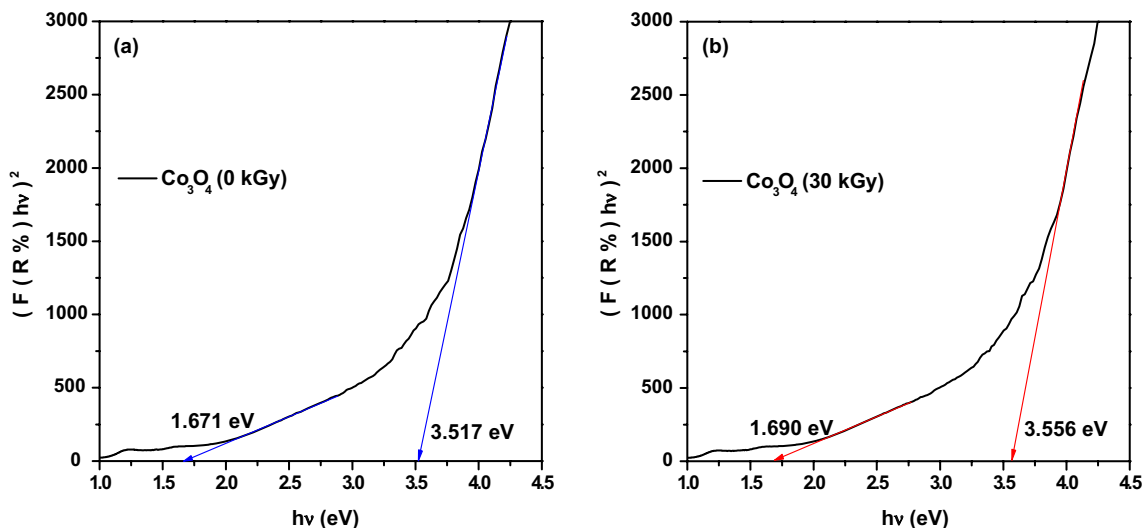
Figure 3. Diffused reflectance spectra of Co_3O_4 nanoparticles versus hυ using Kubelka–Munk function: (**a**) before and (**b**) after irradiating by electron beam radiation at a dose of 30 kGy.

well with previous reports[72–75]. However, these values have been increased to 1.690 eV and 3.556 eV, respectively as Co_3O_4 nanoparticles have been irradiated by electron beam at a dose of 30 kGy. This blue shift could be related to the decreased crystallite size upon irradiation by electron beam which agrees with XRD results. Besides, the quantum confinement effect could also cause this increase in the optical band gap. Additionally, the oxidation effect of electron beam could also be another cause of increasing the band gap as some of Co^{2+} would be converted to Co^{3+} and change their position to the octahedral cites instead of occupying the tetrahedral cites which could perturb the electronic structure of the spinel Co_3O_4 nanoparticles.

<u>Photoluminescence analysis.</u>   The photoluminescence analysis (PL) is inspected to analyze the optical emission properties of Co_3O_4 nanostructures and to confirm the presence of oxygen vacancies in the un-irradiated Co_3O_4 nanoparticles and to compare the spectrum with that of the irradiated Co_3O_4 nanoparticles at a dose of 30 kGy of electron beams.

When excited at 250 nm ($\lambda_{excitation}$), the emission spectrum of un-irradiated Co_3O_4 nanoparticles show a broad peak that has two maxima (Fig. 4), the deeper emission originates at 411 nm which refers to the blue emission whereas the other maximum is at 463 nm which denotes the green emission. The shallow peak that appears at 560 nm is also in the green emission range and reflects the presence of defects and oxygen vacancies within the nanoparticles which is responsible for the stabilization of Co_3O_4 cubic spinel structure, in agreement with previous reports. It is worth noting that blue band is ascribed to the $O^{2-}–Co^{2+}$ charge-transfer process whereas the green emission is related to the $O^{2-}–Co^{3+}$ charge transfer[76]. The deep peak in the blue range and the weak green emission confirm the good crystallinity of our prepared nanoparticles[77].
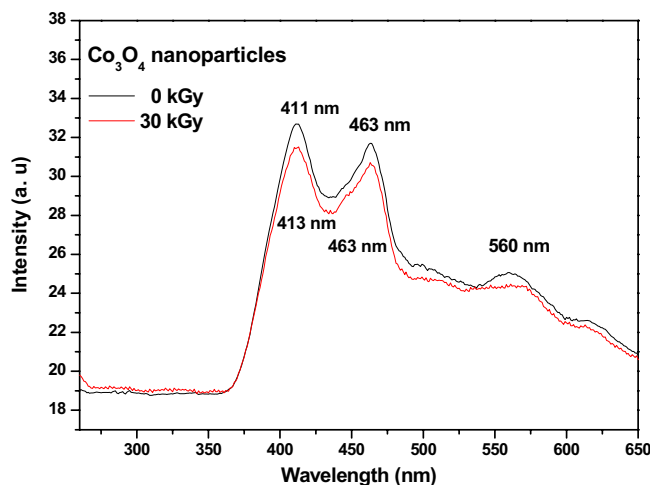

Figure 4. A comparison between photoluminescence spectra for Co_3O_4 nanoparticles before and after irradiation at a dose of 30 kGy of electron beams.

Upon irradiating the samples at a 30 kGy of electron beams, no significant shift on the two main peaks of Co_3O_4 nanoparticles has been observed. However, the shallow peak (at 560 nm) which denotes the presence of the oxygen vacancies has been damped which is suitably related to the oxidation effect of electron beams on the surface Co^{2+} ions.

XPS analysis

To further investigate the alterations on the oxidation states of cobalt ions on the surface of Co_3O_4 nanoparticles upon irradiation, X-ray photoelectron spectroscopy (XPS) was carried out. As shown in Fig. 5a, the Co 2p spectrum of Co_3O_4 nanoparticles before irradiation indicates a low energy and a high energy band at 781.08 eV and 795.08 eV, corresponding to Co $2p_{3/2}$ and Co $2p_{1/2}$, with two satellites at 790.08 eV and 805.08 eV, and these are the characteristic of Co_3O_4 phases[78]. The Co $2p_{3/2}$ peak of 781.08 eV can be further disassembled into two fitting peaks at 780.08 eV and 782.08 eV, and the Co $2p_{1/2}$ peak of 795.08 eV can be further disassembled into two fitting peaks at 795.08 eV and 798.08 eV. The peaks with the binding energy of 780.08 eV and 795.08 eV can be appointed to Co^{3+}, while the peaks at 782.08 eV and 798.08 eV can be appointed to Co^{2+}.

It is observed from Fig. 5b that upon irradiating the Co_3O_4 nanoparticles at a dose of 30 kGy of electron beam, a slight shift of the peaks corresponding to Co^{2+} to higher binding energies. Additionally, the area ratio of surface Co^{2+} against Co^{3+} has decreased from 52.88% to 42.28% which infers that Co^{3+} has become the predominant on the surface and some of Co^{2+} has transformed to Co^{3+} as a result of exposure to electron beam radiation. This could be ascribed to the oxidation effect of the ionizing radiation reported by many researchers, and consequently, some surface oxygen vacancies vanishing. This agrees well with the photoluminescence result which refers to fewer oxygen vacancies on the surface as Co_3O_4 nanoparticles has been irradiated at a dose of 30 kGy of electron beam.

ESR and magnetic analysis

The ESR spectra of Co_3O_4 nanoparticles are investigated at room temperature (300 K) before and after exposure to e-beam at different doses (10, 20, and 30 kGy) as illustrated in Fig. 6. The ESR signal of un-irradiated Co_3O_4 is centered at about 3400 G which is attributed to Co^{2+} ion that have 3d7 electronic configuration. The isotropic g-factor (g) representing the spectroscopic splitting factor and measures the electronic environment around the paramagnetic Co^{2+} ions within the nanoparticles, remains relatively constant around 2.048 before and after irradiation at a dose of 10 kGy. This indicates little change in the electronic environment at the lowest subjected irradiation dose. At irradiation doses of 20 and 30 kGy, the g-factor increases slightly. This suggests that electron beam exposure begins to perturb the electronic environment around the Co^{2+} ions, resulting in a higher g-factor. This is a slight shift of the resonance field to higher magnetic fields upon irradiation. The Δg value, representing the deviation from the free electron g-factor of 2.0023, also increases slightly with higher irradiation doses, confirming the changes to the electronic structure induced by electron beam exposure. Also, its negative sign infers the ionic bonding in Co_3O_4 nanoparticles[79]. The ESR signal intensity, proportional to the number of unpaired electrons, also increases with rising irradiation dose. This indicates that electron beam irradiation generates more free radical species within the nanoparticles. The partial elimination of oxygen vacancies due to exposure to e-beam radiation and freeing of some trapped electrons could be the reason for this increase in the signal intensity[80]. The increase in g-factor, Δg and ESR intensity with higher irradiation doses suggests that electron beam exposure slightly distorts and defects the crystal structure of Co_3O_4, generating more free electrons and paramagnetic centers. It is also observable that the radiation dose has nearly no effect on the signal shape or size which infers that the oxygen vacancies only initiates on the surface so it quickly vanishes upon irradiation and the alteration only appears in the signal intensity.

Table 2 shows trends in the isotropic factor (g), g-shift (Δg) and ESR signal intensity of Co_3O_4 nanoparticles after exposure to different doses of electron beam irradiation. The isotropic factor g remains relatively constant around 2.048, indicating that the electron spin state of the Co_3O_4 nanoparticles is not significantly altered by
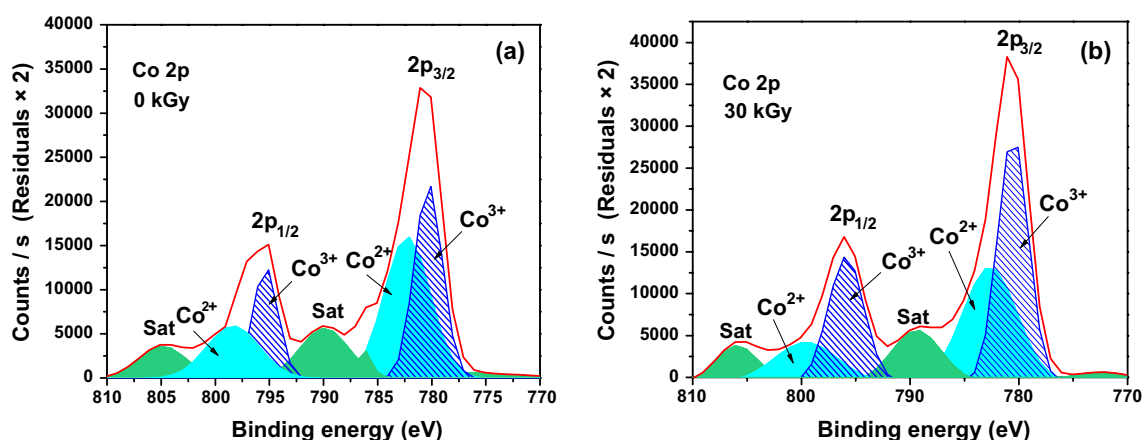

Figure 5. XPS spectra of Co 2p of the Co_3O_4 nanoparticles: (**a**) before and (**b**) after electron beam irradiation at a dose of 30 kGy.
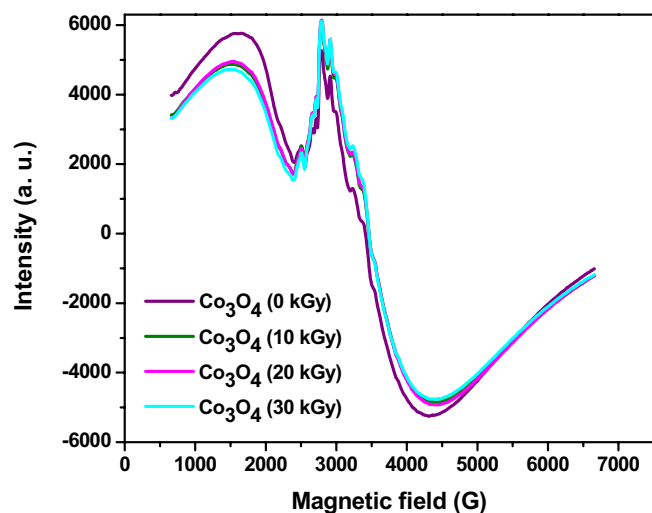
Figure 6. ESR spectra of Co_3O_4 nanoparticles before and after exposure to different doses of electron beam.

Dose (kGy)	g	Δg	Signal intensity (counts/g)
0	2.04807	− 0.04577	99,790.87
10	2.04807	− 0.04577	100,388.17
20	2.04809	− 0.04579	102,954.33
30	2.04818	− 0.04588	106,197.45

Table 2. The isotropic factor, g and signal intensity of Co_3O_4 nanoparticles at different doses of electron beam.

electron beam exposure up to 30 kGy. The g-shift (Δg) shows a small increase with irradiation dose, suggesting a slight change in the electron spin configuration upon electron beam exposure. However, the absolute values of the g-shift remain very small. Most notably, the ESR signal intensity, proportional to the number of unpaired electrons, increases dramatically with electron beam dose. There is a 6% increase in signal intensity from the unirradiated nanoparticles to those exposed to 30 kGy. This data suggests a significant increase in unpaired electrons detected by ESR spectroscopy. This could be due to vanishing oxygen vacancies on the surface of nanoparticles upon irradiation, freeing traped unpaired electrons and, thus a stronger ESR signal.

In summary, electron beam irradiation appears to generate more electron spin centers within Co_3O_4 nanoparticles, as evidenced by the increase in ESR signal intensity with dose, while having little effect on the actual electron spin state, as indicated by the relatively constant g values. The enhanced number of unpaired electrons could influence the magnetic and catalytic properties of the irradiated nanoparticles. This suggests irradiation induces crystallographic distortions, eliminates oxygen vacancies that generate more paramagnetic centers within the Co_3O_4 nanoparticles.

The magnetization measured at room temperature as a function of the applied field (hysteresis loop) for Co_3O_4 nanoparticles before and after exposure to 30 kGy of electron beams is illustrated in Fig. 7. Our investigated Co_3O_4 nanoparticles are characterized by three important parameters; the coercivity (H_c) which represents the strength of the applied magnetic field needed to reduce the nanoparticles' magnetization to zero after saturation, the remanent magnetization (M_r) which refers to the magnetic moment that the nanoparticles retain without an external magnetic field where the non-zero M_r also indicates ferromagnetic behavior, and the saturation magnetization (M_s) which refers to the maximum magnetic moment attained by the nanoparticles when an external magnetic field is applied. It is observed that Co_3O_4 nanoparticles revealed a weak ferromagnetic behavior in which the coercive field (H_c) is 112.57 G, the remanent magnetization (M_r) is 15.076E-3 emu/ g, and the saturation magnetization (M_s) is 0.538 emu/g. The saturation magnetization (which characterizes the ferromagnetic behavior) of previously reported works compared to our work is found in Table 3. Many researchers have reported the ferromagnetic behavior of the nanosized Co_3O_4 particles in converse to its bulk behavior (anti-ferromagnetic)[81,82]. In nanosized materials, the existence of oxygen vacancies which mainly establish on the particles surface is responsible for trapping unpaired electrons, generating ferromagnetic order as their spins will polarize together[83]. Besides, the exchange interaction between Co^{2+} and Co^{3+} ions at the tetrahedral and octahedral sites in spinel Co_3O_4 and the density of states redistribution can influence the magnetic properties of the Co_3O_4[63].

It is also reported that the magnetic properties of Co_3O_4 is affected by its crystal field. In an octahedral field, the five degenerate d orbitals of Co ions split into two sets of orbitals (t_{2g} and e_g) where t_{2g} are three low energy orbitals whereas e_g are two high energy orbitals. The difference between these sets of orbitals depends on the ligand nature; increases with strong ligands. In the presence of strong ligand, the lower orbitals are filled before the higher orbitals and the Co ion will be in low-spin state whereas in the presence of weak field ligand, the
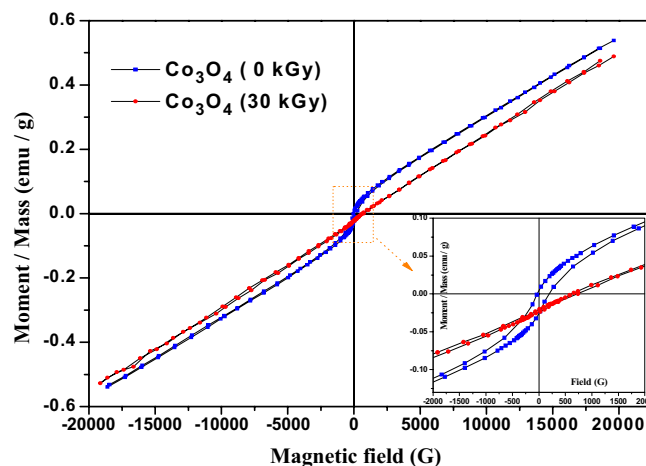
Figure 7. The hysteresis curve of Co_3O_4 nanoparticles before and after irradiation by electron beam at a dose of 30 kGy.

Preparation method	Size (nm)	M_s (emu/g)	References
Co-precipitation method	58	0.813	[84]
Precipitation method	36	0.362	[85]
Thermal decomposition at 175 °C	11	0.137	[86]
Microwave combustion method	45.8	0.005	[87]
Sol–gel method	47.55	0.538	Present work

Table 3. Saturation magnetization of Co_3O_4 nanoparticles prepared at different crystallite sizes by different preparation methods and conditions compared to our result.

electrons fill the orbitals in a Hund's rule type of order and pair up only when they have no other choice and the Co ion will be in a high spin state. In case of a tetrahedral field, the energy levels are reversed and the d orbitals split into two lower lying fully occupied e - states and three half-filled t_2 - states[88], respectively where the difference between these sets of orbitals is nearly half that in case of the octahedral field[89] so, the electrons fill the orbitals in a high spin state regardless of the ligand nature. In the spinel structured Co_3O_4 nanoparticles, the surrounding O ions represent a strong ligand so the magnetic configuration of Co^{3+} that occupy the octahedral sites[90,91] is $S = 0$ ($t_{2g}^6 e_g^0$).

In contrast, the magnetic configuration of Co^{2+} that normally occupy the tetrahedral sites is $S = 3/2$ ($e_g^4 t_{2g}^3$), which confirms that the antiferromagnetic behavior of Co_3O_4 in the bulk case comes from the Co^{2+} ions as a result of their three unpaired electrons[69]. In the nanoscale, as in our system, the presence of magnetic moment is largely related to the oxygen vacancies as well as the crystal symmetry deficiency, since Co^{3+} ions have no magnetic moment[90] and Co^{2+} cancels its total magnetic moment due to its antiferromagnetic nature. However, the observed weak ferromagnetic nature of our system may be related to surface uncompensated Co^{2+} and/or the surface oxygen vacancies that mainly arise in the nanoscale system as a result of the weak coordination on the surface as well as the loss of translational symmetry[83].

However, the irradiated Co_3O_4 nanoparticles (30 kGy) show lower values of these magnetic parameters than those of the un-irradiated Co_3O_4 nanoparticles as shown in Table 4. This could be attributed to oxidation and freeing of some trapped electrons due to irradiation. This behavior agrees with XPS and PL analyses that

Sample	H_c (G)	M_r (emu/g)	M_s (emu/g)	Total area (erg/g)	Squareness (Mr/Ms)
Co_3O_4 (0 kGy)	112.57	15.076E–3	0.538	165.780	27.988E–3
Irradiated Co_3O_4 (30 kGy)	49.51	1.7408E–3	0.508	34.590	3.4254E–3
XLPE/Co_3O_4	175.72	3.9082E–3	72.445E–3	61.470	53.948E–3
Irradiated XLPE/Co_3O_4 (30 kGy)	135.18	857.93E–6	23.644E-3	16.423	36.286E–3

Table 4. Magnetic parameters of Co_3O_4 nanoparticles and XLPE/Co_3O_4 nanocomposite before and after irradiation.

10

concluded the decrease of Co^{2+} ions (responsible for unpaired electrons) and oxygen vacancies on the surface upon irradiation, respectively.

The physiochemical properties of irradiated (XLPE/Co$_3$O$_4$) nanocomposite

As the magnetic and electrical properties of Co_3O_4 nanoparticles could be enhanced by the presence of oxygen vacancies[38,92] so we have chosen the un-irradiated Co_3O_4 nanoparticles, as having the highest oxygen vacancies, to be filled in XLPE and to investigate the structural, optical, magnetic, and electrical properties of the resultant nanocomposite before and after irradiation by electron beams.

XRD

Upon filling the un-irradiated Co_3O_4 nanoparticles in XLPE matrix, the same lattice planes of Co_3O_4 nanoparticles appear with a slight shift from their positions and the peaks concerning XLPE appear around $2\theta = 20°$ (Fig. 8). The XRD pattern of XLPE/Co_3O_4 nanocomposite after irradiation by 30 kGy of the electron beam is also depicted in Fig. 8. The lattice parameters of Co_3O_4 nanoparticles have been calculated as altered after embedding in XLPE matrix. The calculated values are shown in Table 5 for comparison.

From Table 5**,** the Co_3O_4 nanoparticles (0 kGy) have a crystallite size of 47.55 nm and a lattice constant of 8.128 A°. After being embedded in the XLPE matrix, the crystallite size decreases significantly to 18.49 nm. This suggests that the XLPE matrix restricts the growth of the Co_3O_4 nanoparticles. However, the lattice constant increases after embedding in XLPE, indicating some strain induced by the polymer matrix on the nanoparticles. The dislocation density also increases markedly after the Co_3O_4 nanoparticles are embedded in XLPE, from 0.442×10^{15} to 2.925×10^{15} Lines/m². This suggests that the incorporation process induces defects and distortions in the nanoparticles. After irradiation of the XLPE/Co_3O_4 composite with 30 kGy of electron beam, the crystallite size and lattice constant increase slightly to 18.91 nm and 8.216 A°, respectively whereas the dislocation density decreased marginally after 30 kGy irradiation. This could be due to some restructuring (enhanced crystallinity) and growth of the nanoparticles under irradiation. These slight changes in the XRD parameters indicate that the crystal structure of the Co_3O_4 nanoparticles remains relatively stable within the XLPE matrix upon moderate electron beam exposure.

Optical band gap

The optical band gap (E_g) of un-irradiated XLPE and XLPE/Co_3O_4 nanocomposite (before and after irradiation by electron beam) has also been estimated from the diffused reflectance spectra using Kubelka–Munk function (Eq. 4). By plotting $(F(R) h\upsilon)^{1/2}$ versus $h\upsilon$ and extrapolating the linear part of the curve to $F(R) = 0$, the optical
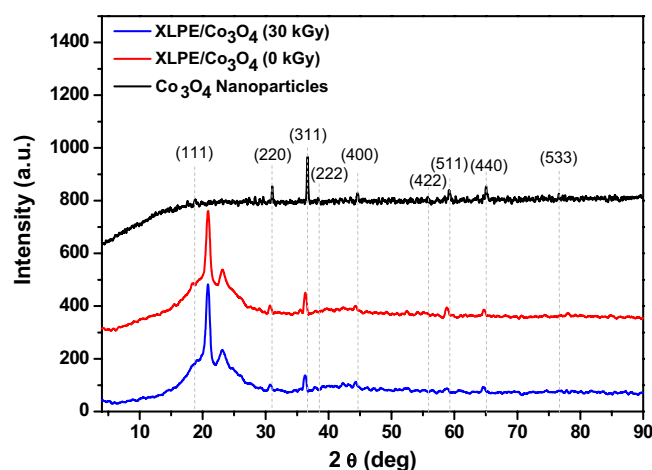

Figure 8. The XRD patterns of XLPE/Co_3O_4 nanocomposite before and after irradiation by 30 kGy of electron beam compared to that of the as prepared Co_3O_4 nanoparticles.

Sample	D (nm)	a (A°)	$\delta \times 10^{15}$ (Lines/m²)
Co$_3$O$_4$ (0 kGy)	47.55	8.128	0.442
XLPE/ Co$_3$O$_4$ (0 kGy)	18.49	8.203	2.925
XLPE/ Co$_3$O$_4$ (30 kGy)	18.91	8.216	2.793

Table 5. XRD calculated parameters of XLPE/Co_3O_4 before and after irradiation at a dose of 30 kGy of electron beam compared to those calculated for un-irradiated Co_3O_4 nanoparticles.

band gap value of the samples could be determined as shown in Fig. 9 and 10. It is observed that XLPE (Fig. 9) shows two indirect optical transitions, the lower one is at 2.08 eV whereas the higher one is at 3.62 eV.

However, upon filling XLPE with Co_3O_4 (Fig. 10), the lower gap slightly decreased to 2.06 eV whereas the higher gap increased to 3.55 eV. This slight shift as Co_3O_4 filled XLPE matrix could be ascribed to the low weight percent (5%) of Co_3O_4 nanoparticles which have also two energy gaps which are relatively lower than these values, the lower one is at 1.671 eV whereas the higher one is at 3.517 eV. It is important to note that the presence of Co_3O_4 nanoparticles introduces additional energy states that can contribute to the observed energy transitions in the nanocomposite. However, upon irradiating XLPE/Co_3O_4 nanocomposite at a dose of 30 kGy of electron beam (Fig. 10), a red shift from these values has been achieved in the lower value which could be attributed to cross linking and imperfections induced by radiation which could decrease the optical band gap[93,94]. However, the higher band gap value of the nanocomposite exposed to 30 kGy exceeds that of the un-irradiated one. The spinel structure of Co_3O_4 with Co^{2+} and Co^{3+} ions distributed across octahedral sites which is responsible for the two different band gaps could be affected by electron beam induced oxidation which consequently would affect both the optical band gaps and the electronic conductivity of the polymeric nanocomposite. The estimated values of the low and high optical band gaps of XLPE and XLPE/Co_3O_4 nanocomposite before and after irradiation at a dose of 30 kGy of electron beam are listed in Table 6 for comparison.

ESR and magnetic analysis
In investigating the ESR results of XLPE/Co_3O_4 nanoparticles, it is observed that the signal related to Co^{2+} ions has disappeared upon filling inside the polymeric matrix (Fig. 11). This could be attributed to the low weight
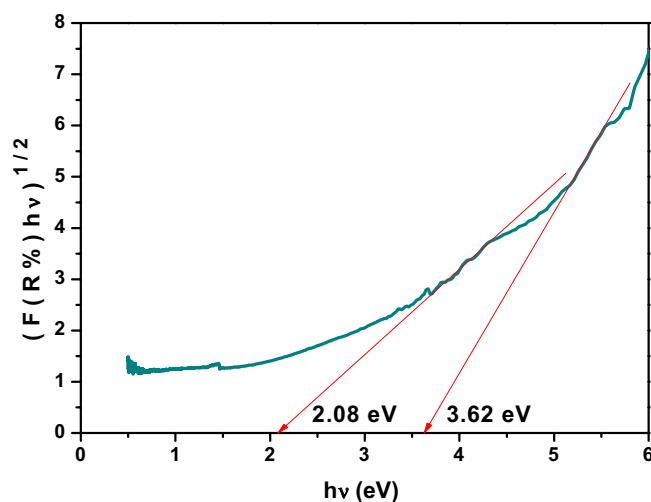

Figure 9. Diffused reflectance spectra of neat XLPE versus hυ using Kubelka–Munk function.
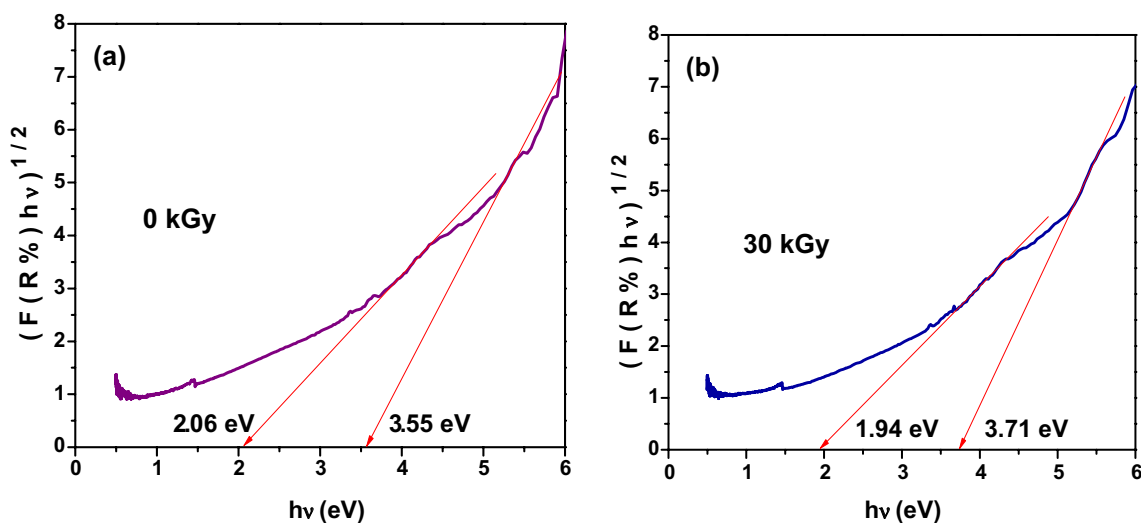

Figure 10. Diffused reflectance spectra of XLPE/Co_3O_4 nanocomposite versus hυ using Kubelka–Munk function: (**a**) before and (**b**) after exposure to electron beam radiation at a dose of 30 kGy.

Sample	E_{g1} (eV)	E_{g2} (eV)
XLPE (0 kGy)	2.08	3.62
XLPE/Co_3O_4 (0 kGy)	2.06	3.55
XLPE/Co_3O_4 (30 kGy)	1.94	3.71

Table 6. Optical band gap values of XLPE/ Co_3O_4 nanocomposite before and after exposure to electron beam radiation at a dose of 30 kGy.
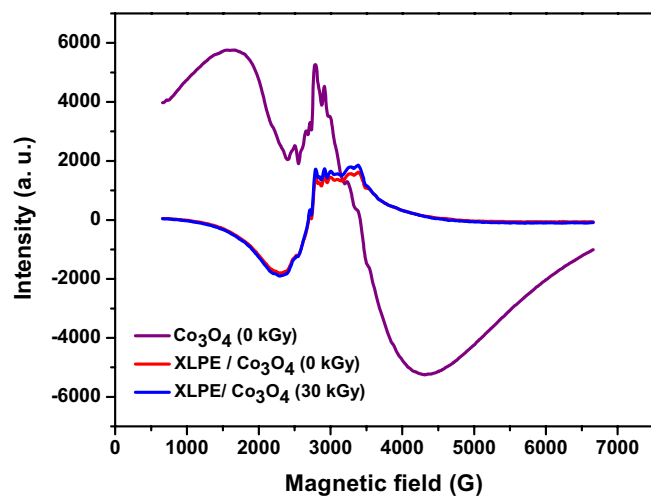

Figure 11. ESR spectra of XLPE/Co_3O_4 nanocomposites before and after electron beam irradiating at a dose of 30 kGy compared to the spectrum of un-irradiated Co_3O_4 nanoparticles.

fraction of the filler (~ 5%) as well as the restriction of surface electrons as embedded in the polymeric XLPE Matrix. It is worth noting that also no signal is observed after irradiating XLPE/Co_3O_4 nanocomposite with 30 kGy of electron beam.

In investigating the magnetization versus magnetic field behavior of XLPE/ Co_3O_4 nanocomposites (Fig. 12), we observe that the nanocomposite has also gained a ferromagnetic behavior but with higher coercive field (H_c) ~ 175.72 G than that of the un-irradiated Co_3O_4 nanoparticles. However, the remanent magnetization (M_r), and saturation magnetization (M_s) are reduced (see Table 4). The nanocomposite's increased coercivity and decreased retentivity may be caused by the polymer chains that restrict the easy response of electrons spin as the sample is magnetized and demagnetized. Additionally, the highly increased dislocation lines density (see Table 5) initiated during the polymerization process could cause domain wall pinning[47]. So, more external field
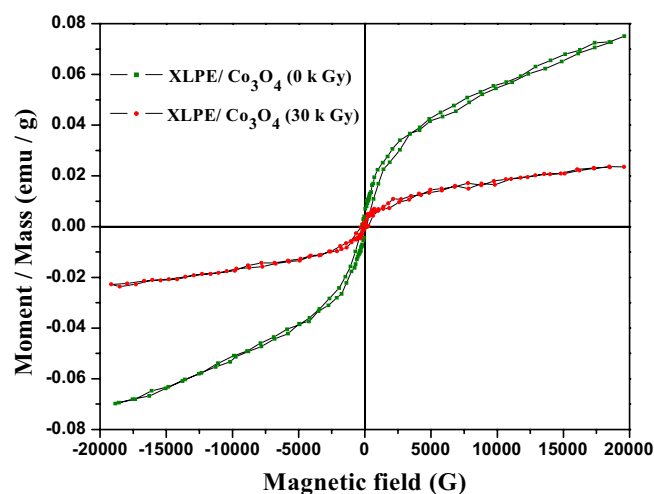

Figure 12. Magnetization versus applied field of XLPE/Co_3O_4 nanocomposite before and after 30 kGy electron beam exposure.

would be exerted to unpin the domain wall from its pinned position and accordingly, the polymeric nanocomposite shows a greater coercivity. As expected, the irradiated nanocomposite (30 kGy) shows lower values of these magnetic parameters related to the oxidation effect of electron beam and the decrease in oxygen vacancies that trap the unpaired electrons. Besides, decreasing dislocation lines density upon irradiating the XLPE/Co_3O_4 nanocomposite at a dose of 30 kGy is also responsible for the decreased coercivity compared to the un-irradiated nancomposite. Also, the smaller area of the nanocomposite hysteresis loop before and after irradiation could be attributed to the low ratio of Co_3O_4 nanoparticles[46] (~ 5%) in the XLPE matrix. The room temperature ferromagnetic behavior with relatively low values of retentivity and coercivity of our prepared nanocomposite before and after irradiation suggests using it as soft magnets which find applications in spintronics.

Dielectric analysis and complex conductivity of XLPE/Co₃O₄ nanocomposite

Figure 13 show the effect of frequency, ranging from 10 to 10^7 Hz at room temperature, on the dielectric permittivity of XLPE/Co_3O_4 nanocomposite before and after irradiation at 0, 10, 20, and 30 kGy of an electron beam. The high dielectric permittivity values (ε') over all range of frequency are due to the semiconducting nature of the Co_3O_4 nanocomposites. These high values have been relatively decreased upon irradiation and the sample exposed to 30 kGy of electron beam shows the least values. Upon exposure to electron beam irradiation, the dielectric permittivity generally decreases. This trend is observed at all frequencies and for all irradiation doses. The sample irradiated with the highest dose of 30 kGy shows the lowest permittivity values over the entire frequency range. The reduction in permittivity upon irradiation suggests that radiation causes defects within the Co_3O_4 nanoparticles and the XLPE polymer matrix. These defects reduce the material's ability to store charge, lowering the dielectric constant. As the irradiation dose increases, more defects are generated, resulting in a further decrease in dielectric permittivity. The 30 kGy sample has accumulated the most defects and thus exhibits the lowest permittivity. The decrease in permittivity with increasing frequency can be attributed to space charge polarization and interfacial polarization effects, which become less prominent at higher frequencies. The electron beam irradiation induces defects within the XLPE/Co_3O_4 nanocomposite that reduce its ability to store charge, decreasing dielectric permittivity. Higher irradiation doses generate more defects and cause a further reduction in permittivity.

Figure 14 portrays the frequency-dependent behavior of the real part of complex conductivity (σ') for the XLPE/Co_3O_4 nanocomposite subjected to varying electron beam irradiation doses (0, 10, 20, and 30 kGy). To provide context, the inset includes the real conductivity of neat XLPE polymer. A discernible transition in conductivity is evident, shifting from a power-law plateau characteristic (σ_{DC}) to another state contingent on frequency (σ_{AC}). This transition, marked by an inflection point, characterizes the response typical of disordered materials, particularly polymers[95].

The σ_{DC} for the unirradiated XLPE/Co_3O_4 sample spans the range of 10^{-3} S/cm $< \sigma < 10^{-2}$ S/cm, indicative of semiconductor behavior. This relatively higher DC conductivity is attributed to the ionic conductivity of Co_3O_4 nanoparticles, rather than electronic conductivity, given the slight reduction in the XLPE's optical band gap upon Co_3O_4 nanoparticle incorporation. Notably, the (111) planes within the Co_3O_4 spinel structure facilitate rapid diffusion paths for charged species, further enhancing ionic conductivity. Increased (111) plane population augments ionic conductivity potential.

Upon irradiation, a subtle rise in both AC and DC conductivity manifests. This phenomenon underscores irradiation's role in liberating charge carriers, enhancing their mobility across XLPE segments rather than inducing changes in electronic structure[96]. In polymers like XLPE, charge transport primarily involves hopping charge carriers (electrons or holes) between molecular chains. Electron beam irradiation incites bond breakage
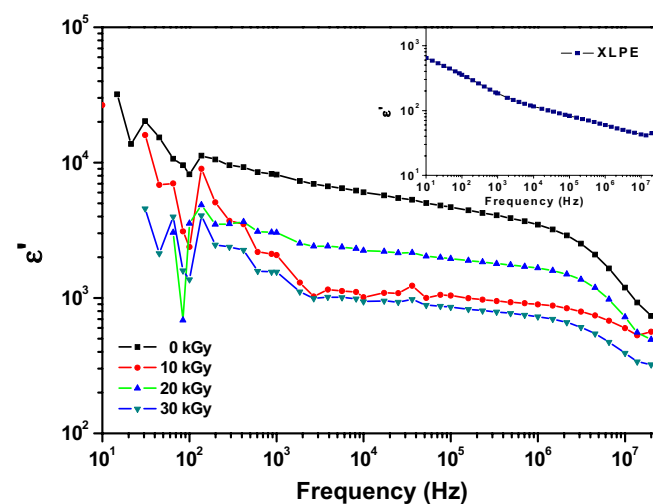

Figure 13. Frequency dependence of real dielectric permittivity ε' of XLPE/Co_3O_4 nanocomposite exposed to different doses of electron beam. The inset shows the dielectric permittivity spectrum of neat XLPE.
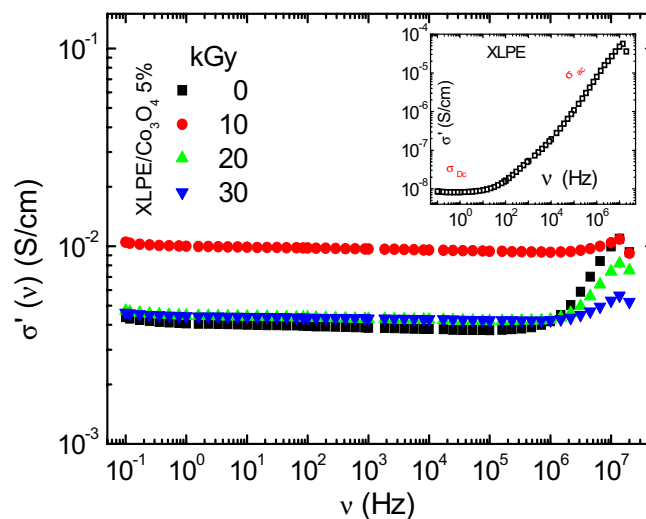
Figure 14. The real part of the conductivity σ′ (ν) as a function of frequency at room temperature for XLPE/Co$_3$O$_4$ nanocomposites exposed to 0, 10, 20, 30 kGy. The σ′ (ν) of neat XLPE film is in the inset.

and defects within XLPE chains, resulting in free electrons and holes as mobile charge carriers. These carriers achieve heightened mobility within polymer segments, no longer restricted to individual molecules. They navigate between defect states created by irradiation, albeit modestly, bolstering AC and DC conductivity.

The abundance of (111) planes with their high atomic density and favorable atomic arrangement engenders optimal diffusion pathways for ions, enhancing ionic conductivity. The hexagonal arrangement within (111) planes facilitates bi-dimensional ion movement, while their low surface energy and stability accommodate ion migration with minimal distortion. This arrangement also entails lower activation energies for ion diffusion. The increased AC conductivity corresponds to the responsiveness of free charge carriers to alternating electric fields at higher frequencies, while the slight DC conductivity rise stems from additional charge carriers contributing to consistent current flow.

In sum, electron beam irradiation of the XLPE/Co$_3$O$_4$ nanocomposite induces defects that promote charge carrier mobility, resulting in a modest increase in AC and DC conductivity. The proliferation of (111) planes enhances ionic conductivity, facilitating charge carrier diffusion and reducing activation barriers. While the overall effect is relatively modest, this irradiation-induced conductivity enhancement holds significant potential for diverse applications necessitating improved charge transport and material performance**.**

Impedance spectroscopic study of XLPE/Co$_3$O$_4$ nanocomposite
The Nyquist impedance plots at room temperature (RT) for neat XLPE and XLPE/Co$_3$O$_4$ nanocomposites before and after exposure to varying electron beam doses are depicted in Fig. 15a and 15b, respectively. All samples exhibit semi-circular patterns intersecting the X-axis, indicative of impedance predominantly influenced by the
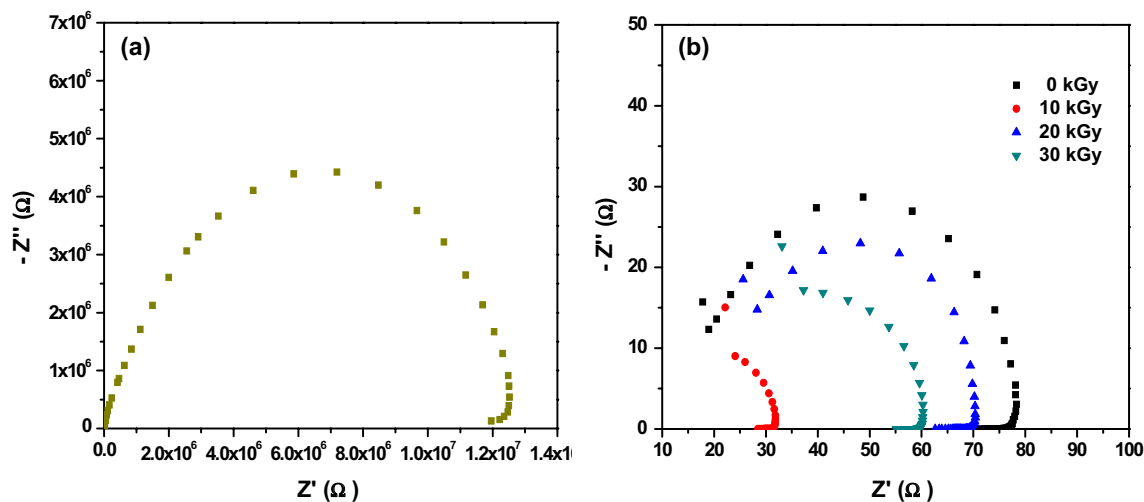

Figure 15. Nyquist impedance plot for (**a**) neat XLPE and (**b**) XLPE/Co$_3$O$_4$ nanocomposite at different doses of electron beam.

Sample	σ (S/cm)
XLPE (0 kGy)	0.133×10^{-7}
XLPE/Co$_3$O$_4$ (0 kGy)	2.198×10^{-3}
XLPE/Co$_3$O$_4$ (10 kGy)	6.258×10^{-3}
XLPE/Co$_3$O$_4$ (20 kGy)	3.262×10^{-3}
XLPE/Co$_3$O$_4$ (30 kGy)	3.614×10^{-3}

Table 7. The conductivity values of un-irradiated XLPE and XLPE/Co$_3$O$_4$ composites before and after irradiation, as calculated from the impedance spectra.

material's bulk resistance (R$_b$) and capacitance (C). This characteristic signifies the contribution of bulk properties rather than solely surface effects.

The intercepts on the real axis at the lower frequency range denote the specimens' bulk resistance (R$_b$), where lower R$_b$ corresponds to higher conductivity[97,98]. The [111] planes within Co$_3$O$_4$ host an elevated density of under coordinated cobalt atoms, serving as active sites for electron conduction. The presence of Co$_3$O$_4$ nanoparticles shifts the semicircles towards higher frequencies, indicating diminished R$_b$ and augmented conductivity compared to neat XLPE. The conductivity of the polymer nanocomposites was calculated through Eq. (5) from the complex impedance spectra (Fig. 15) and the calculated values are listed in Table 7.

As depicted in Table 7 and Fig. 15, the DC conductivity has increased upon filling XLPE by Co$_3$O$_4$ nanoparticles; approximately multiplied by the fourth power of ten. However, a slight increase in DC conductivity is observed upon irradiation. Owing to the high ionic conductivity of transition metal oxides[99], filling XLPE with Co$_3$O$_4$ nanofiller would cause a reasonable overall ionic conductivity of the polymer nanocomposite which could be applied as a good solid electrolyte. It is worth noting that XLPE/Co$_3$O$_4$ (10 kGy) possessed the higher Dc conductivity (6.258×10^{-3} S/cm).

Significantly, the [111] planes of Co$_3$O$_4$ play a pivotal role in ameliorating conductivity. Exposure to electron beam radiation further shifts the semicircles to higher frequencies, underscoring a more pronounced reduction in R$_b$ and an intensified enhancement in conductivity. This is attributed to the ability of active sites on the [111] planes of Co$_3$O$_4$ to trap the additional electrons and holes produced by radiation, thereby facilitating charge transport.

The combined effect of Co$_3$O$_4$ nanoparticles and electron beam radiation synergistically contributes to the amplified DC conductivity of the nanocomposites. The [111] planes, characterized by their rich concentration of active sites, significantly drive this mechanism. Consequently, the unique interplay between Co$_3$O$_4$ nanoparticles, [111] plane exposure, and electron beam radiation establish an intricate yet effective pathway for boosting conductivity within the XLPE/Co$_3$O$_4$ nanocomposites.

Conclusion

This study demonstrates the multifaceted impacts of electron beam irradiation on Co$_3$O$_4$-based nanocomposites and highlights the potential for tailoring their properties through controlled manipulation. The findings underscore the promise of such nanocomposites in applications ranging from enhanced electrical conductivity to potential usage as solid electrolytes, while shedding light on their structural, optical, magnetic, and electrical transformations under electron irradiation.

In the pursuit of developing nanocomposites, nanosized ferromagnetic Co$_3$O$_4$ particles were synthesized using the sol–gel method and subsequently incorporated into the XLPE matrix. As explored by ESR, the electron beam irradiation of Co$_3$O$_4$ nanoparticles led to increased free un-paired electrons. This phenomenon suggests that the irradiation process has induced oxidation of surface Co^{2+} ions which leads to partial elimination of oxygen vacancies, freeing the trapped electrons and generating an elevated number of unpaired electrons, confirmed by XPS and PL techniques, respectively. As the oxygen vacancies are mainly responsible for the weak ferromagnetic behavior of Co$_3$O$_4$ nanoparticles, the irradiated Co$_3$O$_4$ nanoparticles at a dose of 30 kGy showed lesser saturation magnetization (0.508 emu/g) than the un-irradiated Co$_3$O$_4$ nanoparticles (0.538 emu/g).

In investigating the magnetic behavior of XLPE/Co$_3$O$_4$ nanocomposite, prepared via melt extrusion, a weak ferromagnetic behavior is observed which is characterized by low coercivety ~ 175.72 G which further decreased to 135.18 G upon irradiating the nanocomposite at a dose of 30 kGy of electron beam. However, both values are higher than that of the un-irradiated Co$_3$O$_4$ nanoparticles ~ 112.57 G. The highly increased dislocation lines density initiated during the polymerization process could cause pinning of the domain wall. So, more external field would be exerted to unpin the domain wall from its pinned position and accordingly, the polymeric nanocomposite before and after irradiation showed greater coercivities. The room temperature ferromagnetic behavior with relatively low coercivity values of our prepared nanocomposite before and after irradiation suggests using it as soft magnets which find applications in spintronics. On the other hand, comprehensive optical and dielectric analyses reveal the semiconducting nature of the nanocomposite, evidenced by the range of its two indirect optical band gap (2.06 and 3.55 eV), and high dielectric permittivity. The influence of varying electron beam doses on the electrical properties of the nanocomposite has also been explored. A marginal yet notable augmentation in AC and DC conductivity is observed post-irradiation. Incorporating Co$_3$O$_4$ nanofillers into XLPE has boosted its conductivity from 0.133×10^{-7} S/m to 2.198×10^{-3} S/cm which is ascribed to the ionic conductivity of the resultant polymer nanocomposite. Upon exposure to a 30 kGy dose of electron radiation, this conductivity further increases to 3.614×10^{-3} S/cm, showcasing the potential utility of this nanocomposite as a solid electrolyte.

Data availability

The data that support the findings of this study are available from the corresponding author on request.

References

1. Wuttig, M. *et al.* Revisiting the nature of chemical bonding in chalcogenides to explain and design their properties. *Adv. Mater.* **35**(20), 2208485 (2023).
2. Younis, S. A., Ghobashy, M. M. & Samy, M. Development of aminated poly (glycidyl methacrylate) nanosorbent by green gamma radiation for phenol and malathion contaminated wastewater treatment. J. Environ. Chem. Eng. **5**, 2325–2336 (2017).
3. Younis, S. A., Ghobashy, M. M., & Samy, M. Development of aminated poly (glycidyl methacrylate) nanosorbent by green gamma radiation for phenol and malathion contaminated wastewater treatment. Journal of environmental chemical engineering, **5**(3), 2325-2336. (2017)
4. Hou, Z. *et al.* Lattice-strain engineering for heterogeneous electrocatalytic oxygen evolution reaction. *Adv. Mater.* **35**, 2209876 (2023).
5. Ghobashy, M. M., & Elhady, M. A. Radiation crosslinked magnetized wax (PE/Fe3O4) nano composite for selective oil adsorption. Comp. Comm., **3**, 18-22. (2017)
6. Leitenstorfer, A. *et al.* The 2023 terahertz science and technology roadmap. *J. Phys. D Appl. Phys.* **56**(22), 223001 (2023).
7. Guselnikova, O. *et al.* "Functional upcycling" of polymer waste towards the design of new materials. *Chem. Soc. Rev.* https://doi.org/10.1039/D2CS00689H (2023).
8. Ghobashy, M. M. & Khafaga, M. R. Chemical modification of nano polyacrylonitrile prepared by emulsion polymerization induced by gamma radiation and their use for removal of some metal ions. J. Polym. Environ. **25**, 343–348 (2017).
9. Xie, A. *et al.* Oxygen vacancy mediated polymerization of pyrrole on MoO_3 to construct dielectric nanocomposites for electromagnetic waves absorption application. *J. Alloy Compd.* **938**, 168523 (2023).
10. Bawazeer, O. *et al.* A review on using nanocomposites as shielding materials against ionizing radiation. *J. Umm Al-Qura Univ. Appl. Sci.* **9**, 1–16 (2023).
11. Pinto, G. M. *et al.* From two-dimensional materials to polymer nanocomposites with emerging multifunctional applications: A critical review. *Polym. Compos.* **44**(3), 1438–1470 (2023).
12. Assad, H. *et al.* Overview and fundamentals of polymer nanocomposites. In *Nanocomposites-Advanced Materials for Energy and Environmental Aspects* 41–66 (Elsevier, 2023).
13. Ghamsarizade, R., Ramezanzadeh, B. & Mohammadloo, H. E. A review on recent advances in 2D-transition metal carbonitride-MXenes nano-sheets/polymer composites' electromagnetic shields, mechanical and thermal properties. *J. Taiwan Inst. Chem. Eng.* **144**, 104740 (2023).
14. Mohammed, I. & Srivastava, A. Polymer-nanoferrite composites: Structural, transport, and magnetic properties. In *Magnetic Nanoferrites and their Composites* 117–140 (Elsevier, 2023).
15. Abdalla, T. H. *et al.* Fabrication of sustainable hydrogels-based chitosan Schiff base and their potential applications. *Arab. J. Chem.* **15**(1), 103511 (2022).
16. Lian, J.-J., Guo, W.-T. & Sun, Q.-J. Emerging functional polymer composites for tactile sensing. *Materials* **16**(12), 4310 (2023).
17. Kyomuhimbo, H. D. & Feleni, U. Electroconductive green metal-polyaniline nanocomposites: Synthesis and application in sensors. *Electroanalysis* **35**(2), e202100636 (2023).
18. Ghobashy, M. M. *et al.* Gamma irradiation induced surface modification of (PVC/HDPE)/ZnO nanocomposite for enhancing the oil removal and conductivity using COMSOL multiphysics. *Sci. Rep.* **13**(1), 1–13 (2023).
19. Sharshir, A. I. *et al.* Impact of γ-irradiation and SBR content in the compatibility of aminated (PVC/LLDPE)/ZnO for improving their AC conductivity and oil removal. *Sci. Rep.* **12**(1), 19616 (2022).
20. Abdelhamied, M. *et al.* Chemical deposition of Ag and Ag_2O on grafting film of PET-COOH by photografting polymerization for optoelectronic application. *J. Mater. Sci. Mater. Electron.* **34**(1), 41 (2023).
21. Khalaf, A. *et al.* Influence of macromolecular additives on mechanical properties of polyether sulfone and polysulfone ultrafiltration membranes. *Desalin. Water Treat.* **100**, 29–37 (2017).
22. Wang, Y. *et al.* Effect of nanoparticle surface modification and filling concentration on space charge characteristics in TiO_2/XLPE nanocomposites. *J. Nanomater.* **2016**, 1–10 (2016).
23. Mohamed, T., Faraj, S. & Judran, H. Electrical treeing behavior in XLPE insulation due to content AL_2O_3 nanoparticles. *J. Phys. Conf. Ser.* https://doi.org/10.1088/1742-6596/1973/1/012010 (2021).
24. Sharshir, A. *et al.* Simulating the electric field distribution in medium-voltage cables of cross-linked polyethylene/Cu nanocomposites irradiated by E-beam with reference to the XLPE market. *Plast. Rubber Compos.* **51**(6), 281–292 (2022).
25. Ashish Sharad, P. & Kumar, K. S. Application of surface-modified XLPE nanocomposites for electrical insulation-partial discharge and morphological study. *Nanocomposites* **3**(1), 30–41 (2017).
26. Madani, L. *et al.* Investigation of dielectric behavior of water and thermally aged of XLPE/$BaTiO_3$ composites in the low-frequency range. *Int. J. Mod. Phys. B* **29**(27), 1550186 (2015).
27. Sharshir, A. *et al.* Experimental investigation of E-beam effect on the electric field distribution in cross-linked polyethylene/ZnO nanocomposites for medium-voltage cables simulated by COMSOL Multiphysics. *J. Anal. Sci. Technol.* **13**(1), 16 (2022).
28. Wang, Y. *et al.* Effect of nano-MgO doping in XLPE on charge transport and electric field distribution in composite insulation of HVDC cable joint. *Energies* **15**(19), 6948 (2022).
29. Jassim, H. H. & Hashim, F. S. Synthesis of (PVA/PEG: ZnO and Co_3O_4) nanocomposites: Characterization and gamma ray studies. *NeuroQuantology* **19**(4), 47 (2021).
30. Al-Gharram, M., et al. *PANI-CSA/Co_3O_4 Nanocomposite Films: Optical, Morphological, and Structural Properties*. In *2nd International Conference on Industry 4.0 and Artificial Intelligence (ICIAI 2021)* (Atlantis Press, 2022).
31. Esmaeili Bidhendi, M. *et al.* New magnetic Co_3O_4/Fe_3O_4 doped polyaniline nanocomposite for the effective and rapid removal of nitrate ions from ground water samples. *Environ. Progr. Sustain. Energy* **39**(1), 13306 (2020).
32. Kale, V. N. & Maiyalagan, T. Interface engineering of ZIF-67 derived heterostructured CeO_2@Co_3O_4 polyhedron promoted by reduced graphene oxide for enhanced oxygen evolution reaction. *J. Alloys Compd.* **961**, 170887 (2023).
33. Sharma, D. *et al.* Transition metal phosphide nanoarchitectonics for versatile organic catalysis. *Small* **19**(11), 2207053 (2023).
34. Choudhary, S. *et al.* Microwave-assisted facile fabrication of α-Fe_2O_3/$CoFe_2O_4$/Co_3O_4 ternary nanohybrids with highly enhanced photocatalytic activity. *Opt. Mater.* **132**, 112836 (2022).
35. Galini, M., Salehi, M. & Behzad, M. Structural, magnetic and dielectric properties of pure and Dy-doped Co_3O_4 nanostructures for the electrochemical evolution of oxygen in alkaline media. *J. Nanostruct.* **8**(4), 391–403 (2018).
36. Yin, K. *et al.* Magnetic properties of Co_3O_4 nanoparticles on graphene substrate. *J. Alloys Compd.* **720**, 345–351 (2017).
37. Dalapati, G. K. *et al.* Tin oxide for optoelectronic, photovoltaic and energy storage devices: A review. *J. Mater. Chem. A* **9**(31), 16621–16684 (2021).

38. Leel, N. *et al.* Oxygen vacancy driven luminescence, ferromagnetic and electronic structure properties of Eu doped CeO_2 nanoparticles. *J. Lumin.* **263**, 119981 (2023).

39. Wang, X., Yu, M. & Feng, X. Electronic structure regulation of noble metal-free materials toward alkaline oxygen electrocatalysis. *eScience* **3**, 100141 (2023).

40. Liu, M. *et al.* Confine activation peroxymonosulfate by surface oxygen vacancies of BiO1– xCl to boost its utilization rate. *Sep. Purif. Technol.* **307**, 122711 (2023).

41. Elbasiony, A. *et al.* Tailoring the linear and nonlinear optical properties of PVC/PE blend polymer by insertion the spindle copper nanoparticles. *Opt. Mater.* **148**, 114811 (2024).

42. Elbasiony, A. *et al.* Preparation and multifaceted characterization and optoelectronic potential of $Cu/CuO/Cu_2O$ nanoplates in a PVC/PE matrix. *J. Mater. Sci. Mater. Electron.* **35**(3), 194 (2024).

43. Ganguly, S. & Margel, S. 3D printed magnetic polymer composite hydrogels for hyperthermia and magnetic field driven structural manipulation. *Progr. Polym. Sci.* **131**, 101574 (2022).

44. Zhu, X. *et al.* Linear and nonlinear optical properties of Co_3O_4 nanoparticle-doped polyvinyl-alcohol thin films. *Opt. Mater. Express* **2**(1), 103–110 (2012).

45. Bhatt, A. S. & Bhat, D. K. Crystallinity, magnetic and electrochemical studies of PVDF/Co_3O_4 polymer electrolyte. *Mater. Sci. Eng. B* **177**(2), 127–131 (2012).

46. Nandapure, B., Kondawar, S. & Nandapure, A. Magnetic properties of nanostructured cobalt and nickel oxide reinforced polyaniline composites. *Int. J. Comput. Appl.* **2**, 9–14 (2012).

47. Wassel, A. R. *et al.* Impact of Sm_2O_3 on the morphological, optical, magnetic, and pesticide adsorption of Co_3O_4/PANI hybrid nanocomposites. *ECS J. Solid State Sci. Technol.* **11**(8), 083009 (2022).

48. Fan, Y. *et al.* PANI-Co_3O_4 with excellent specific capacitance as an electrode for supercapacitors. *Ceram. Int.* **47**(6), 8433–8440 (2021).

49. Ramezani, M. *et al.* Surface engineering of metals: Techniques, characterizations and applications. *Metals* **13**(7), 1299 (2023).

50. Kogularasu, S. *et al.* Nanofibers: Empowering electrochemical sensors for reliable detection of food and environmental toxins. *J. Electrochem. Soc.* **170**(7), 077514 (2023).

51. Tomboc, G. M. *et al.* Defect-induced electronic modification and surface reconstruction of catalysts during water oxidation process. *Chem. Eng. J.* **454**, 140254 (2023).

52. Mendes, P. C. *et al.* Opportunities in the design of metal@ oxide core-shell nanoparticles. *Adv. Phys. X* **8**(1), 2175623 (2023).

53. Scherrer, P. Bestimmung der Grosse und inneren Struktur von Kolloidteilchen mittels Rontgenstrahlen. *Nach Ges Wiss Gottingen* **2**, 8–100 (1918).

54. Asadi, A. *et al.* Modification of hexachiral unit cell to enhance auxetic stent performance. *Mech. Adv. Mater. Struct.* **30**(7), 1470–1484 (2023).

55. Jiao, C. *et al.* Experimental research on a novel soil displacement monitoring system based on measurement unit cells (MUCs). *Measurement* **211**, 112605 (2023).

56. Li, Y. *et al.* Local measurement of geometrically necessary dislocation densities and their strengthening effect in ultra-high deformed pearlite. *Mater. Charact.* **203**, 113132 (2023).

57. Demir, E. *et al.* A finite element method to calculate geometrically necessary dislocation density: Accounting for orientation discontinuities in polycrystals. *Acta Mater.* **245**, 118658 (2023).

58. Kubelka, P. Ein beitrag zur optik der farbanstriche. *Z. Tech. Phys* **12**, 593–601 (1931).

59. Zhang, L. *et al.* In-situ characterization of silicate slag crystallization by electrical impedance spectroscopy: Construction of continuous cooling transformation diagram. *Mater. Charact.* **197**, 112648 (2023).

60. Sahoo, R. R. & Choudhary, R. Structural, dielectric and impedance spectroscopy analysis of green phase rare earth cuprates Gd2BaCuO5 and Dy2BaCuO5. *J. Inorg. Organomet. Polym. Mater.* **33**, 1–18 (2023).

61. Bennie, R. B. *et al.* Electrical conductivity and electrochemical studies of Cr-doped MoO_3 nanoflakes for energy storage applications. *J. Solid State Electrochem.* **27**(1), 271–280 (2023).

62. Sharma, P. & Sharma, A. Structural & magnetic properties of cobalt oxide nanoparticles at different annealing temperatures. *Int. J. Mater. Sci. Eng.* **4**, 208–214 (2016).

63. Kupchak, I. & Serpak, N. Electronic and magnetic properties of spinel Co_3O_4 (111) surface in GGA+ U approximation. *Ukr. J. Phys.* **62**(7), 615–615 (2017).

64. Sun, D. *et al.* Biomorphic composites composed of octahedral Co3O4 nanocrystals and mesoporous carbon microtubes templated from cotton for excellent supercapacitor electrodes. *Appl. Surf. Sci.* **465**, 232–240 (2019).

65. Wen, Z. *et al.* Flower-shaped C-Dots/Co_3O_4 111 constructed with dual-reaction centers for enhancement of fenton-like reaction activity and peroxymonosulfate conversion to sulfate radical. *Catalysts* **11**(1), 135 (2021).

66. Wen, Z., et al., *Flower-Shaped C-Dots/Co3O4 {111} Constructed with Dual-Reaction Centers for Enhancement of Fenton-Like Reaction Activity and Peroxymonosulfate Conversion to Sulfate Radical. Catalysts 2021, 11, 135.* 2021, s Note: MDPI stays neutral with regard to jurisdictional claims in published.

67. Qin, C. *et al.* Crystal-plane-dependent Fischer-Tropsch performance of cobalt catalysts. *ACS Catal.* **8**(10), 9447–9455 (2018).

68. Song, K., Cho, E. & Kang, Y.-M. Morphology and active-site engineering for stable round-trip efficiency Li–O_2 batteries: A search for the most active catalytic site in Co_3O_4. *ACS Catal.* **5**(9), 5116–5122 (2015).

69. Cadi-Essadek, A. *et al.* DFT+ U study of the electronic, magnetic and mechanical properties of Co, CoO, and Co_3O_4. *S. Afr. J. Chem.* **74**(1), 8–16 (2021).

70. Zhang, H. *et al.* In situ atomic-scale observation of silver oxidation triggered by electron beam irradiation. *Nanomaterials* **11**(4), 1021 (2021).

71. Ghoranneviss, M., et al. *Electron beam modification of polypropylen fabrics*. In *Proc. of the 3rd International Conference on the Frontiers of Plasma Physics and Technology (PC/5099), P-15, Tehran, Iran* (2007).

72. Vennela, A. *et al.* Structural and optical properties of Co_3O_4 nanoparticles prepared by sol-gel technique for photocatalytic application. *Int. J. Electrochem. Sci.* **14**(4), 3535–3552 (2019).

73. Muradov, M. *et al.* The effect of Cu doping on structural, optical properties and photocatalytic activity of Co_3O_4 nanoparticles synthesized by sonochemical method. *Opt. Mater.* **142**, 114001 (2023).

74. Makhlouf, S. A. *et al.* Structural, electrical and optical properties of Co_3O_4 nanoparticles. *Superlattice Microstruct.* **64**, 107–117 (2013).

75. Shariffudin, S. *et al.* Effect of film thickness on structural, electrical, and optical properties of sol-gel deposited layer-by-layer ZnO nanoparticles. *Trans. Electr. Electron. Mater.* **13**(2), 102–105 (2012).

76. Anandhababu, G. & Ravi, G. Facile synthesis of quantum sized Co_3O_4 nanostructures and their magnetic properties. *Nano-Struct. Nano-Objects* **15**, 1–9 (2018).

77. Al-Tuwirqi, R. *et al.* Facile synthesis and optical properties of Co_3O_4 nanostructures by the microwave route. *Superlattice Microstruct.* **49**(4), 416–421 (2011).

78. Duan, Q. & Chen, H. Synthesis and electrochemical properties of Co_3O_4 nanoparticles by hydrothermal method at different temperatures. *IOP Conf. Ser. Mater. Sci. Eng.* https://doi.org/10.1088/1757-899X/207/1/012020 (2017).

79. Farouk, M., *ESR, IR and Optical Absorption Studies of Co2+ ions in ZnO-PbO-B2O3 glass System.*

80. Xiao, Y. *et al.* Regulating the pore structure and oxygen vacancies of cobaltosic oxide hollow dodecahedra for an enhanced oxygen evolution reaction. *NPG Asia Materials* **12**(1), 73 (2020).
81. Ullah, A. A., Amin, F. B. & Hossain, A. Tailoring surface morphology and magnetic property by precipitants concentrations dependent synthesis of Co_3O_4 nanoparticles. *Ceram. Int.* **46**(17), 27892–27896 (2020).
82. Zhu, H. *et al.* Synthesis and magnetic properties of antiferromagnetic Co_3O_4 nanoparticles. *Phys. B Condens. Matter* **403**(18), 3141–3145 (2008).
83. Al-Senani, G. M., Deraz, N. M. & Abd-Elkader, O. H. Magnetic and characterization studies of CoO/Co_3O_4 nanocomposite. *Processes* **8**(7), 844 (2020).
84. Abdallah, A. & Awad, R. Study of the structural and physical properties of Co_3O_4 nanoparticles synthesized by co-precipitation method. *J. Supercond. Novel Magn.* **33**, 1395–1404 (2020).
85. Prabaharan, D. D. M. *et al.* Precipitation method and characterization of cobalt oxide nanoparticles. *Appl. Phys. A* **123**, 1–6 (2017).
86. Farhadi, S., Safabakhsh, J. & Zaringhadam, P. Synthesis, characterization, and investigation of optical and magnetic properties of cobalt oxide (Co_3O_4) nanoparticles. *J. Nanostruct. Chem.* **3**, 1–9 (2013).
87. Sundararajan, M. *et al.* Study of physical and magnetic properties of Mg: Co_3O_4 spinels using ʟ-arginine as fuel. *J. Ovonic Res.* **17**(5), 479–486 (2021).
88. Upton, T. H. & Goddard, W. A. III. The electronic states of Ni2 and Ni2+. *J. Am. Chem. Soc.* **100**(18), 5659–5668 (1978).
89. Lohaus, C. *et al.* Investigations on RF-magnetron sputtered Co_3O_4 thin films regarding the solar energy conversion properties. *J. Phys. D Appl. Phys.* **49**(15), 155306 (2016).
90. Ichiyanagi, Y. & Yamada, S. The size-dependent magnetic properties of Co_3O_4 nanoparticles. *Polyhedron* **24**(16–17), 2813–2816 (2005).
91. Gawali, S. R. *et al.* Role of cobalt cations in short range antiferromagnetic Co_3O_4 nanoparticles: A thermal treatment approach to affecting phonon and magnetic properties. *Sci. Rep.* **8**(1), 249 (2018).
92. Yang, S. *et al.* Oxygen-vacancy abundant ultrafine Co_3O_4/graphene composites for high-rate supercapacitor electrodes. *Adv. Sci.* **5**(4), 1700659 (2018).
93. Maity, T. & Sharma, S. Effect of gamma radiation on optical and electrical properties of tellurium dioxide thin films. *Bull. Mater. Sci.* **31**, 841–846 (2008).
94. Arshak, K. & Korostynska, O. Gamma radiation dosimetry using tellurium dioxide thin film structures. *Sensors* **2**(8), 347–355 (2002).
95. Mohamed, F., Ahmad, M. M. & Hameed, T. A. Greener synthesis of lightweight, self-standing $PMMA/CoFe_2O_4$ polymeric film for magnetic, electronic, and terahertz shielding applications. *Polym. Adv. Technol.* **34**(5), 1497–1514 (2023).
96. Karbovnyk, I. *et al.* Effect of radiation on the electrical properties of PEDOT-based nanocomposites. *Nanoscale Res. Lett.* **11**, 1–5 (2016).
97. Thakur, V. N. *et al.* High temperature dielectric and impedance spectroscopy study of LaCo0. 7Nb0. 3O3. *Mater. Res. Bull.* **158**, 112070 (2023).
98. Mandal, B. & Mitra, P. Grain growth correlated complex impedance spectroscopy, modulus spectroscopy and carrier hopping mechanism in $MnCo_2O_4$: Influence of sintering temperature. *Mater. Chem. Phys.* **251**, 123095 (2020).
99. Sarma, B. *et al.* Synergistic enhancement in the capacitance of nickel and cobalt based mixed oxide supercapacitor prepared by electrodeposition. *Appl. Surf. Sci.* **300**, 29–36 (2014).

Author contributions

All authors contributed substantially to the conception and design of the work and to the analysis and interpretation of the data. All authors contributed to revisions and approved the final draft. All authors agree to be accountable for all aspects of the work in ensuring that any questions related to the accuracy or integrity of any part of the work are appropriately investigated and resolved. Specific individual contributions in addition to the above: M.M.G. led the drafting of the paper and contributed to data extraction. A.I.S. contributed to literature searching and data extraction. R.A.Z. contributed to literature searching, data extraction, and drafting sections of the manuscript. F.M. contributed to data extraction and preparation of figures and tables. The lead author M.M.G., the manuscript's guarantor, affirms that the manuscript is an honest, accurate and transparent account of the study being reported. No important aspects of the study have been omitted; and that any discrepancies from the study as planned (and, if relevant, registered) have been explained.

Funding

Competing interests

The authors declare no competing interests.

Additional information

Correspondence and requests for materials should be addressed to M.M.G. or A.I.S.

Reprints and permissions information is available at www.nature.com/reprints.

Publisher's note Springer Nature remains neutral with regard to jurisdictional claims in published maps and institutional affiliations.